# Morphological modeling of a metal foam SOFC configuration

David Masson, Bassam Abdallah, François Willot, Dominique Jeulin, Elisa Mercadelli, Alessandra Sanson, Anthony Chesnaud, Alain Thorel

# Morphological modeling of a metal foam SOFC configuration

D. Masson*, B. Abdallah†, F. Willot†, D. Jeulin*†, E. Mercadelli‡, A. Sanson‡, A. Chesnaud†, A. Thorel†

*Centre for Materials, Mines ParisTech, PSL, UMR CNRS 7633, BP 97, 91003 Évry Cedex, France

† Centre for Mathematical Morphology, Mines ParisTech, PSL Research University, 35 rue S$^{t}$ Honoré, 77300 Fontainebleau Cedex, France

‡ ISTEC, Via Granarolo 64, 48018 Faenza (RA), Italy

**Abstract**

The present paper refers to an innovative SOFC concept named EVOLVE after a running FP7 project which integrates advanced materials and an inventive anode current collector made from a NiCrAl preoxidized foam impregnated with a conductive perovskite. Even if the concept is the beneficial combination of Metal supported cell (MSC) and Anode supported cell (ASC) technologies, strong improvements in terms of reliability and durability are expected. In order to enhance anode efficiency, the 3D microstructure needs to be precisely described at the microscopic scale. ISTEC has produced LST-GDC active anode layers using screen printing process. Back-scattered electrons (BSE) SEM images that contain relevant microstructure information have been realized by Centre des Matériaux. All the original images have been enhanced by Centre de Morphologie Mathématique using a series of morphological operators to remove artefacts. Finally, a 3D pluri-Gaussian model has been generated from 2D images, and then computed to predict volume fraction of the 3 phases, 3D tortuosity, gas permeation and ionic conductivities.

## 1 Introduction

### 1.1 Context

Global warming is always associated to the emission of greenhouse gases coming from industry, transportation and agriculture. Since the last two decades, zero emission energy systems have being developed to limit the greenhouse gases impact on the climate change and secondly to replace the fossil energy which has reached a maximum price of $147.02/barrel in 2008. Hydrogen energy is one of the most promising energy that could be transformed directly into electricity, water and heat. Solid Oxide Fuel Cells (SOFCs) are one of the most attractive and efficient conversion devices to reach around 60% of pure electrical efficiency to 80% if the waste heat is used as cogeneration. SOFCs do not need any noble metals as electrode catalysts and may use a large variety of fuels (hydrocarbons, CO and bio-fuels, hydrogen). Such system can be made for a small portable power unit such as Auxiliary Power Units (APU) to a big size combined heat and power units (CHP) usually used for stationary application. SOFCs have to face critical challenges in terms of short durability, low reliability and higher cost. High operating temperatures are mostly affecting the durability and the reliability both related to inter-diffusion, Ni coarsening and agglomeration, sulphur tolerance, mechanical robustness and chemical stability under redox cycling in temperature. In the last decades, three main configurations have been successively investigated and developed, respectively the Electrolyte Supported Cell (ESC), Anode Supported Cell (ASC) and the Metal Supported Cell (MSC), to improve the performance and the durability (Fig. 1).

### 1.2 Objectives

The main objective of this project is to combine the benefits of the ASC and MSC configurations, respectively high reliability and a good durability. The idea was to use a porous metal supported

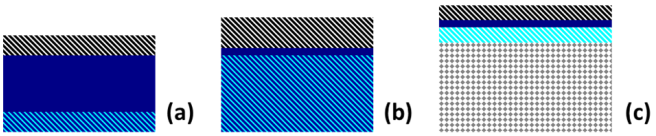


Figure 1: (a) Electrolyte supported cell (ESC), (b) Anode supported cell (ASC), (c) Metal supported cell (MSC).

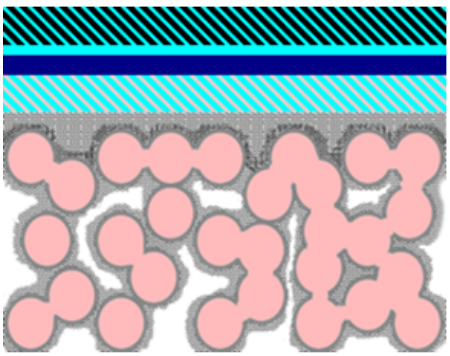

Figure 2: The metallic foam supported cell.

cell impregnated with an anode material and create a porous current collector as support. One of the priorities of the project was to remove the nickel at the anode, to avoid any Ni diffusion and coarsening in the active anode layer. Innovative anode materials were introduced at the anode side instead of nickel, such as $La_{0.10}Sr_{0.90}TiO_{3-\delta}$ (LST) with $Ce_{1-x}Gd_xO_{2-\delta}$ (CGO) composite which have shown in the literature a good catalytic performance in the normal operating conditions (1), (2).

In order to enhance the electrode efficiency, the 3D microstructure needs to be precisely described at the microscopic scale by a morphological model. An optimized microstructure (controlled pores size, morphology and connectivity, grains size distribution, 3D tortuosity and 3D percolation of phases, volume fraction of phases, final thickness of components, ...) is closely related to the starting parameters (nature and quantity of starting powder, binder, shaping aids...) and to the control of the shaping process parameters (sintering treatment and atmosphere). It should meet the best compromise between a good electrocatalytic activity and a low ohmic resistivity while ensuring satisfactory long term thermomechanical stability on the life span of the device. Based on a mathematical morphology approach applied on symmetrical LST-GDC anode layers, the present work aims at showing how a morphology model can be established and 3D microstructural data relevant for shaping and performances can be derived from back-scattered electrons (BSE) SEM observations. For each sample, a series of images were used as input information for the microstructural modeling. All the original images were first filtered to remove the noise, thresholded and finally a series of morphological operators (openings, surface openings, closings and reconstruction with markers) were applied to remove artefacts. A 3D pluri-Gaussian model has been generated from 2D images, and then computed to predict volume fraction of the 3 phases, 3D tortuosity, gas permeation and ionic conductivities.

## 2 Experimental

Commercially available $Sr_{0.90}La_{0.10}TiO_{3-\delta}$ (LST, Cerpotech, Norway) and $Ce_{1-x}Gd_xO_{2-\delta}$ (GDC, Treibacher, Austria) with specific surface area of, respectively, 6.34 $m^2g^{-1}$ and 9.10 $m^2g^{-1}$ were used as starting materials. For the inks production, terpineol was considered as solvent, Phospholan PE65 as dispersant whereas ethyl cellulose (EC, Fluka, Italy) and carbon black (Thermax-Cancarb, USA) were added as binder and pore former respectively. The pore former was the 30 vol.% in respect of the powder. The ink was initially prepared via ball milling and then milled in a three-roll mill equipped

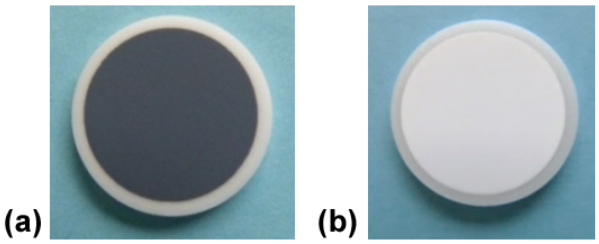


Figure 3: (a) A screen-printing symmetrical cell and (b) sintered symmetrical cell.

with zirconia rollers of nanometric finishing (Exakt 80E, Germany). The symmetrical cells were finally produced depositing the ceramic ink onto each YSZ disc ($\oslash = 18.6$ mm) sides with an automatic screen printer (AUR'EL 900, AUR'EL Automation s.p.a., Italy) and sintered in air at 1000°C or 1100°C for 5 hours. The resulting cells were constituted by 5 to 15 µm thick electrodes, separated by a 1900 µm thick YSZ electrolyte.

In order to determine the anode microstructure, symmetrical cells were cut in 2 pieces, and the half-cell was placed on its cross section in a resin and dry overnight. Secondly, the enrobed samples were polished using a SiC polishing paper (400, 800, 1200, 2500 and 4000), corresponding to a grain size from 30 to 5 µm. Then, a fine polishing step was used to optimize the quality of the image, with micrometrics grains solutions (10, 5, 2 µm). Finally, a last polishing step was realized on each cross section by an Acid Alumina Oxide Suspension (OPS-AA), which removes the last smallest scratches on the surface. The surface of the polishing samples was metalized with 1.5 nm $Au - Pd$ coating under vacuum. Finally, the samples were analyzed with a FEI Nova NanoSEM 450. The contrast between the 3 phases was obtained by back-scattered electrons (BSE) SEM images, using the average atomic number of each phase (Z(LST) = 190.20 $g.mol^{-1}$, Z(GDC-10) = 173.01 $gmol^{-1}$). Low voltage allows to keep the real shape of the particles without affecting the contrast between the 3 phases. Secondly, BSE image of the anode microstructure has to be simplified by only 3 contrast levels, corresponding to one grey level for each phase. A brightness/contrast ratio has been adjusted to get the best optimized segmentation, and kept it constant between each sample.

# 3 Results and discussions

LST-GDC anode layers have been screen-printing on YSZ pellets on both side, and sintered at 1000°C or 1100°C for 5 hours (Fig. 3). The carbon black has been perfectly removed, and perfect flat and crack free layers were obtained on each side.

Three main samples have been compared in this paper, with a change of composition ($LST - GDC10$ and $LST - GDC20$) and a change of sintering temperature (1000°C/5h or 1100°C/5h). These two parameters have an effect on the final microstructure, thus on the performance of the cell. The three microstructures are presented on Fig. (4).

Anode layers are made of ceramic materials that present an electric insulating behavior at room temperature. Even if a thin conducting Au-Pd has been coated on the surface, the sample remains isolating, and complicates the imaging with an electron microscope. By using screen printing process, 5 µm to 15 µm anodic layers have been manufactured. The fine microstructure needs high magnifications for the best segmentation and threshold. Three main magnifications ($\times$10000, $\times$15000, $\times$20000) have been tried to have the best compromise between resolution and noise. An important noise appears for the highest magnification image whereas the resolution is too low for the lowest magnification. The best magnification was chosen as $\times$15000, equivalent to a width of 12.7 µm or 12.4 nm per pixel (Fig. 5).

The images were acquired by a contrast phase detectors at different voltages as shown on Fig. 6. The comparison shows that the particles shape is clearly affected by high voltage, due to a higher penetration of the incident electron beam into the sample. In fact, the BSE detector is really sensitive to the volume of the interaction probe which could change the reflected beam and finally the observed

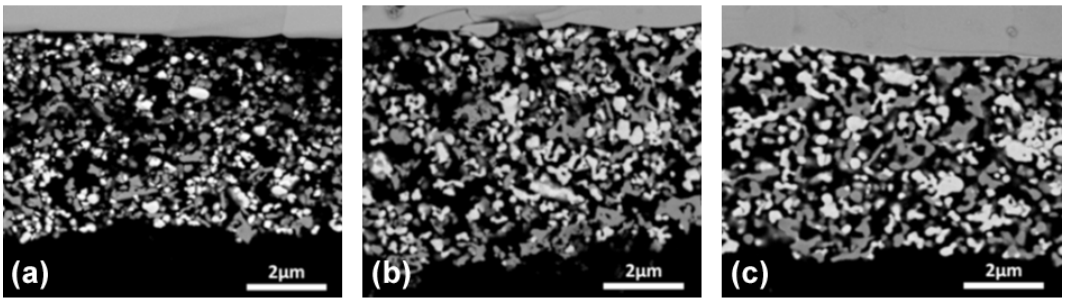


Figure 4: (a) LST − GDC10 and (b) LST − GDC20 sintered at 1000°C for 5 hours, (c) LST − GDC20 sintered at 1100°C for 5 hours.

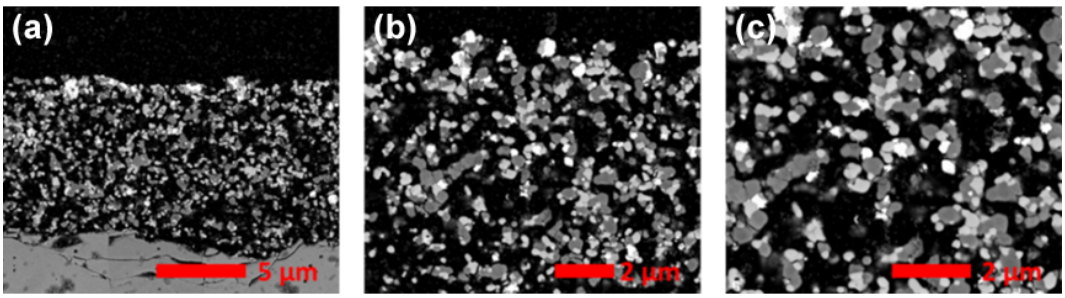


Figure 5: BSE-SEM cross-section of LST-GDC layer at (a) ×10000, (b) ×15000 and (c) ×20000.

shape. This comparison demonstrates how a high voltage decreases the contrast between LST and GDC phases. Actually, the scattered beam coming from the interaction probe volume to the detector has a longer interaction distance for high voltage than for low voltage. Finally, a voltage of 5 kV was chosen for the acquisition of the LST-GDC layers images.

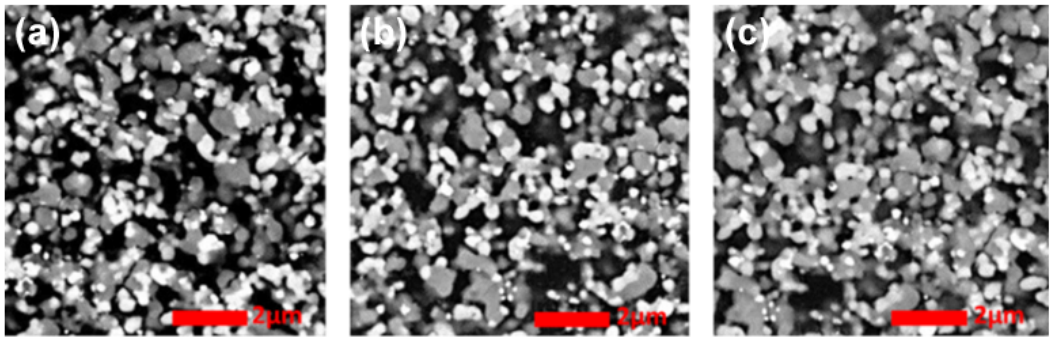


Figure 6: BSE-SEM images recorded at (a) 5 kV, (b) 10 kV and (c) 15 kV.

# 4 Morphological modeling and transport properties

This section is devoted to the morphological modeling of the anode layers and to transport properties predictions. Emphasis is put on image analysis techniques (Sec. 4.1) and the effect of segmentation on the phase volume fractions. The material is reconstructed in 3D using a morphological approach previously developed in [3]. The method, briefly reminded in Sec. (4.2), relies on a generic model

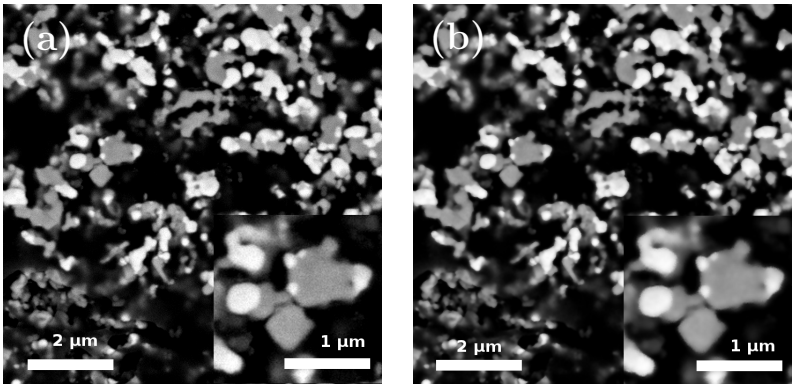


Figure 7: LST-GDC layer: detail of a SEM (a) and filtered image (b) using the bilateral transform (1). Bottom-right, incrusted images: magnification by a factor 2.

appropriate to three-phases material and has been validated using a set of morphological measurements, including the covariance function. A parametrization of the model is proposed in Sec. (4.2). The covariance function used to generate 3D models is approached by a simple analytical formula. Numerical predictions of the material's transport properties are presented in Sec. (4.3).

## 4.1 Image analysis

The pores and solid phases are first separated from each other (i.e., segmented). In the SEM images, the GDC and LST phases appear in white and dark-grey. With pores in black, the three phases have high, intermediate and low pixel values, respectively. Thresholding out the images, however, leads to poor results, for any choice of the threshold (not shown), and smoother images are sought for. Use is made of the classical bilateral filter [4] which removes noise from an image while preserving contours, by the transform:

$$f'(\mathbf{x}) = k(\mathbf{x}) \int_{\mathbf{x}'} \mathrm{d}^2\mathbf{x}' f(\mathbf{x}') r(\mathbf{x}-\mathbf{x}') s(f(\mathbf{x})-f(\mathbf{x}')), \qquad k(\mathbf{x}) = \left[ \int_{\mathbf{x}'} \mathrm{d}^2\mathbf{x}' r(\mathbf{x}-\mathbf{x}') s(f(\mathbf{x})-f(\mathbf{x}')) \right]^{-1} \tag{1}$$

where $f(\mathbf{x})$ is the SEM image at point $\mathbf{x}$, $f'(\mathbf{x})$ the filtered image, and the integration is carried out on all points $\mathbf{x}'$ in the domain. Transform (1) ressembles a convolution product with some important differences. The functions $r$ and $s$ are user-choosen weight functions defined on the spatial domain and pixel values, respectively. The weights become small when points $\mathbf{x}$ and $\mathbf{x}'$ are far apart *or* when the difference between their pixel values is large. Functions $r$ and $s$ are commonly chosen to be Gaussians, i.e. they decrease exponentialy. Transform (1) accordingly performs an averaging of the pixel values in a (spatial) neighborhood of $\mathbf{x}$, but also along the grey-scale itself, which favors pixels with the same value as $f(\mathbf{x})$. It has the same effect as a standard low-pass filter in a smooth region but acts as a more selective filter near the contours between the phases. In these regions indeed, the transform picks pixels that (presumably) lie in the same phase. The normalizing factor $k(\mathbf{x})$ is chosen so that the sum of the weights is constant for each pixel (the reader is refered to refs. [5] and [6] for more details on bilateral filters). The forms of the functions $r$ and $s$, provided in [3], were empiricaly chosen. Results are shown in Fig. (7) for a SEM image of LST-GDC20 sintered at 1100° C. At normal scale, the effect of filtering is hardly noticeable. When magnified, however, noise has disappeared on the filtered image, but the contours remain well-preserved.

The previous filtering allows one to segment the SEM images by simple thresholding. Two thresholds $(\chi_1;\chi_2)$ $(\chi_1 \leq \chi_2)$ are used to separate the three phases. Recall that the two solid phases have the same volume fraction. This leaves one free parameter to be chosen on. Various values of the threshold $\chi_1$ are explored in the range $[0;255]$ and compared visually to the original SEM image. Results are provided in Fig. (8a-d), to be compared with the original image in Fig. (7a). On the one hand, a low value $\chi_1 = 80$ leads to the appearance of LST material that lies in the background. This undesirable

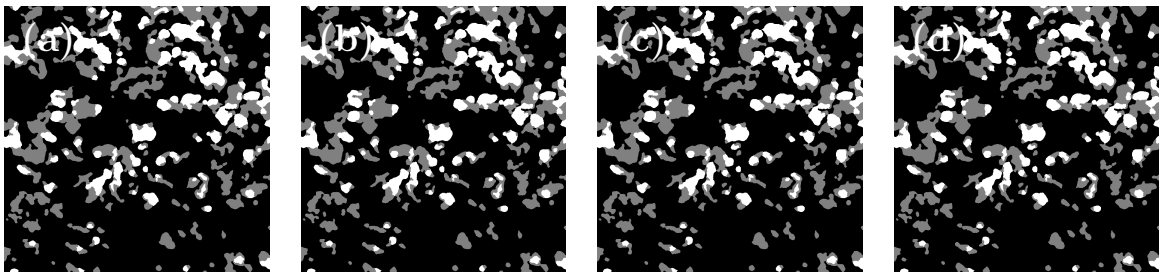


Figure 8: Thresholding of the filtered SEM image of a LST-GDC layer. The result of increasing threshold values $\chi = 80$, 120, 130 and 140 are represented in (a), (b), (c) and (d), respectively.

| $\chi_1$ | 80 | 100 | 120 | 130 | 140 |
|---|---|---|---|---|---|
| Pores vol. fract. (%) | 67 | 71 | 75 | 77 | 80 |
| LST vol. fract. (%) | 19 | 16 | 13 | 12 | 11 |
| GDC vol. fract. (%) | 14 | 13 | 12 | 10 | 9 |

Table 1: Pores, LST and GDC volume fractions obtained with various values of the threshold $\chi_1$ in the range $0 \leq \chi_1 \leq 255$.

effect results from the relief (or 3D) view of the SEM images (Fig. 8a). On the other hand, high threshold values lead to an over-segmentation of the porous phase (Fig. 8d). Optimal segmentation, with respect to the simple two-steps method considered here, is obtained in the intermediate range $120 \lessapprox \chi_1 \lessapprox 130$. A careful visual inspection of the images leads to the choice $\chi_1 = 120$ but quite clearly, some other choices are possible. The effect of the choice of the threshold on the volume fractions of the three phases is given in Tab. (1). As shown in this table, the change in volume fractions of the three phases is not larger, in absolute values, than 2 or 3% in the range of interest $120 \leq \chi_1 \leq 130$. This gives a relative precision of 3, 8 and 17% for the estimate of the pores, LST and GDC volume fractions, respectively.

A third step is necessary to correct artifacts inherent to the segmentation of three-phases media. Contours between the brightest (GDC) and darkest (pores) phases are under-represented. Since pixels along these borders have intermediate values, they are often detected as elongated light-grey regions (i.e., LST) [7]. In our case, a combination of dilation and opening, detailed in [3], suffices to remove the spurious objects.

## 4.2 Three phases pluri-Gaussian model

The main idea for modeling the three-phases material consists in representing each phase $\Omega^{(i)}$ ($i = 1$, 2, 3) by combinations of two underlying sets $X$ and $Y$:

$$\text{GDC} = \Omega^{(1)} = X, \qquad \text{LST} = \Omega^{(2)} = X^{\text{c}} \cap Y, \qquad \text{Pores} = \Omega^{(3)} = X^{\text{c}} \cap Y^{\text{c}}. \tag{2}$$

Conversely, it is easy to exhibit two sets $X$ and $Y$ satisfying the above. Hereafter, however, we assume that the two sets $X$ and $Y$ are *independant random sets*. This strong assumption can be tested in several ways. In particular, the independancy hypothesis allows one to link the covariances $C_{X,Y}$ of $X$ and $Y$ to the covariances $C_{ii}$ and cross-covariances $C_{ij}$ of the $\Omega^{(i)}$, which can be measured:

$$C_X(\mathbf{h}) = P\left\{\mathbf{x}, \mathbf{x}+\mathbf{h} \in X\right\}, \qquad C_Y(\mathbf{h}) = P\left\{\mathbf{x}, \mathbf{x}+\mathbf{h} \in Y\right\}, \qquad C_{ij}(\mathbf{h}) = P\left\{\mathbf{x} \in \Omega^{(i)}, \mathbf{x}+\mathbf{h} \in \Omega^{(j)}\right\}. \tag{3}$$

One obtains:

$$C_{11}(h) = C_X(h), \quad C_{22,33}(h) = C_{X^{\text{c}}}(h) C_{Y,Y^{\text{c}}}(h), \quad C_{12}(h) = C_Y(0)\left[C_X(0) - C_X(h)\right], \tag{4}$$

where, for simplicity, all functions are taken as isotropic and depend on the norm $h = |\mathbf{h}|$ and $C_{X^{\text{c}},Y^{\text{c}}}(h) = 1 - 2C_{X,Y}(0) + C_{X,Y}(h)$ are the covariances of the complementary sets $X^{\text{c}}$ and $Y^{\text{c}}$.

Eliminating the covariances $C_{X,Y}$ from the above, necessary conditions are obtained on the covariances and cross-covariances $C_{ij}(h)$, namely:

$$C_{1j}(h) = \frac{C_{jj}(0)\,[C_{11}(0) - C_{11}(h)]}{1 - C_{11}(0)} \quad (j = 2, 3), \quad C_{23}(h) = \frac{C_{22}(0)\,[1 - 2C_{11}(0) + C_{11}(h)]}{1 - C_{11}(0)} - C_{22}(h). \tag{5}$$

The above equations have been verified to a satisfying degree [3]. In fact, form (2) is one of 6 possible sets of combinations, of which (2) is the most realistic. Again, the reader is refered to [3] for more details.

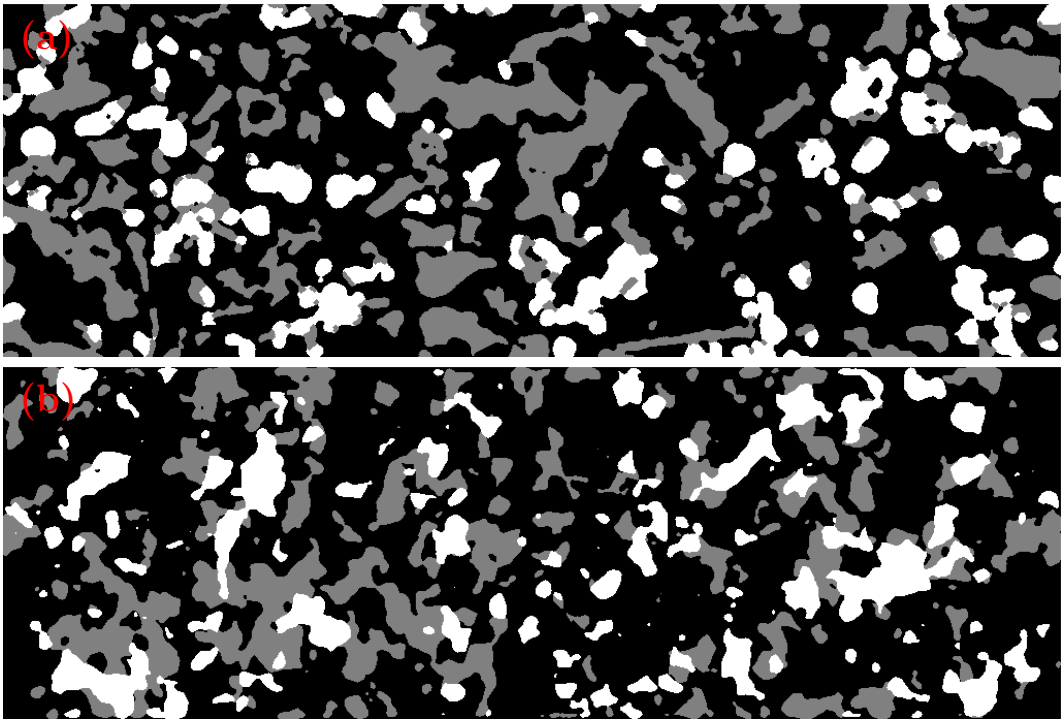


Figure 9: Segmented SEM image (a) and pluri-Gaussian model (b).

Hereafter truncated Gaussian models are used for the underlying sets $X$ and $Y$ [8, 9, 10]. The latter are especially useful for generating sets with smooth boundaries. They are generated numericaly knowing the covariances of sets $X$ and $Y$, provided by (4). For e.g. set $X$, the procedure consists in a numerical inversion of the formula:

$$C_X(h) = \frac{1}{2\pi} \int_0^{\rho(h)} \frac{1}{\sqrt{1 - t^2}} e^{\frac{-\lambda^2}{1+t}} \,\mathrm{d}\, t, \qquad \lambda = F^{-1}(1 - f_X), \tag{6}$$

where $f_X = f_{\mathrm{GDC}}$ is the volume fraction of $X$, $F$ is the cumulative probability function of the normal distribution $\mathcal{N}(0, 1)$ and $\rho(h)$ is the correlation function determined numericaly. The random set $X$ is then generated using:

$$\rho(h) = (w * w)(h) \quad \leftrightarrow \quad w = FFT^{-1}\left(\sqrt{FFT(\rho)}\right), \tag{7}$$

$$X = \{\mathbf{x}; Z_X(\mathbf{x}) \geq \lambda\}, \qquad Z_X(\mathbf{x}) = (w * U)(\mathbf{x}), \qquad U(\mathbf{x}) \sim \mathcal{N}(0, 1), \tag{8}$$

where $*$ is the convolution product, FFT are (fast) Fourier transforms and $U(\mathbf{x})$ is an uncorrelated Gaussian field. To obtain smooth contours we replace the weight function $w$ with:

$$w'(h) = (w * \mathcal{K})(h), \tag{9}$$

where $\mathcal{K}$ is a Gaussian kernel [3]. The same procedure is repeated for set $Y$.

The material and model are visually very close to each other (Fig. 9). Although the method relies on the sole covariances, it provides very good estimates for the granulometries as well as linear erosions [3]. For conciseness, these comparisons are not presented here, but a 3D view of the material is shown in Fig. (10a). Using these models, fine microstructural parameters can be computed, such as tortuosity $\tau$ [14]. The latter is defined as the length of the minimal path (i.e. the geodesic) lying in a given phase and connecting two opposite borders, normalized by the Euclidean distance between the borders. For most anode samples, we obtain $\tau \approx 1.05 \pm 0.02$, $1.57 \pm 0.05$ and $1.68 \pm 0.07$, for the pores, LST and GDC phases, respectively.

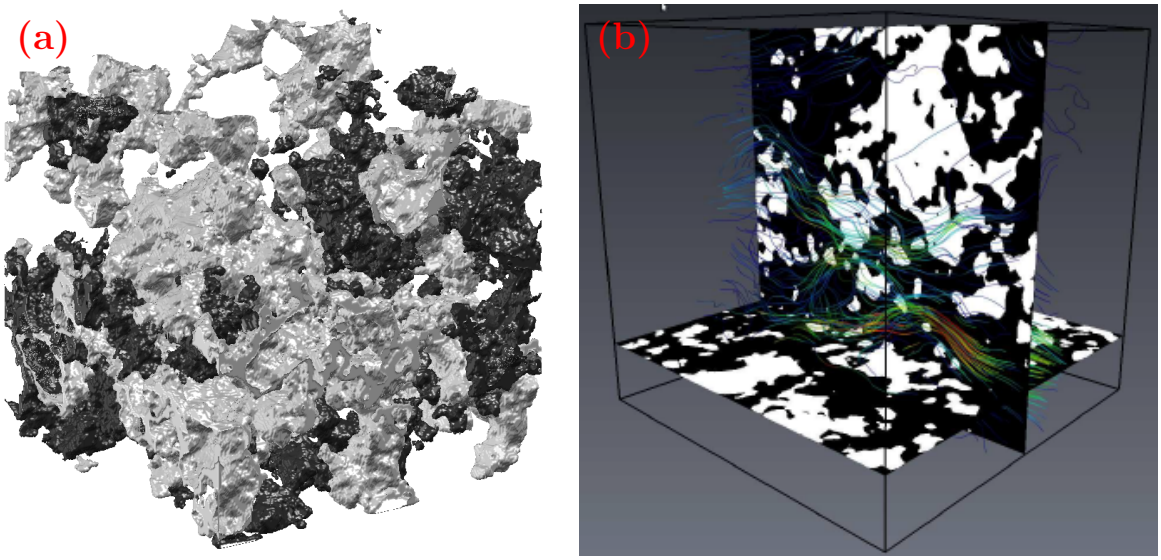


Figure 10: 3D view of the reconstructed model (a) made of GDC (light grey) and LST (dark grey). Pores are transparent. (b) Gaz flow occuring in the porosity of a (model of) GDC10 anode cell layer.

Finally, a useful parametrization of the model is mentioned. The numerical weight functions $w(h)$ are close to the following law:

$$w(h) = \mathrm{e}^{-\sqrt{h/\alpha}}, \tag{10}$$

where $\alpha > 0$. The fit above is very close to SEM image measurements, for most materials, as shown in Fig. (11), which represents the quantity $\log\left[-\log w(h)\right]$ vs. $\log h$.

## 4.3 Transport properties

Ionic conductivity as well as gaz permeation are computed on a 3D model of GDC10 anode layer, using full-field Fourier computations. For ionic conductivity, the "parcimonious" algorithm proposed in [11] is used, whereas for gaz flow, we use the algorithm in [12]. For the GDC phase with local ionic conductivity $4.5\,10^{-4}$ (S/m), we obtain effective ionic conductivities of about $2.4\,10^{-4}$ (S/m).

For Stokes flow, an effective permeability computed on three samples gives $3.5\,10^{-11}$ to $5.6\,10^{-11}$ ($\mathrm{cm}^2$) for four materials with 61 to 65% volume of pores. It is useful to compare these values to that of an ideal Boolean model of spherical obstacles [13]. Specifically, the anode layers have the same permeability as a Boolean model of spheres of diameter roughly 1 µm. This value is consistent with the size of the pores in the anode layers. A 3D view of the streamlines (gaz flow) occuring in the porosity is shown in Fig. (10b). The streamlines are directly computed using the full-field FFT computations. Fig. (10b) illustrates the strong heterogeneity of the streamlines, concentrated around a few major paths.

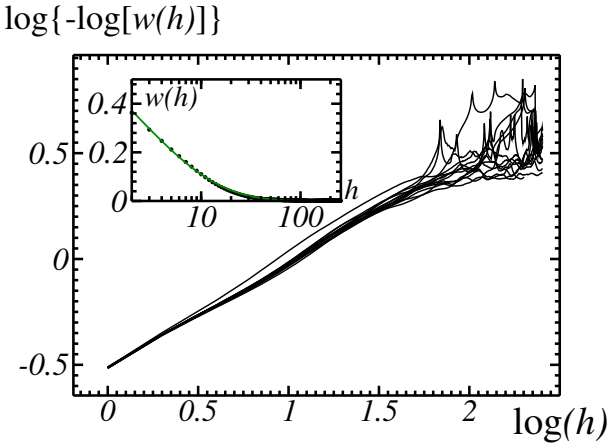


Figure 11: Quantity $\log[-\log w(h)]$ vs. $\log h$, computed on a set of 12 SEM images of anode layers. Top-right, incrusted: weight function $w(h)$ determined from (4), (6) and (7), for one anode layer. Solid line: fit $w(h) = \mathrm{e}^{-\sqrt{h/2.0}}$ with parameter $\alpha = 2.0$ pixels $\approx 25$ nm.

# 5 Conclusion and prospects

A general method has been proposed to model 3D anode cell layers using 2D SEM images. The essential ingredients of the method, beyond image analysis techniques, are the use of two independant pluri-Gaussian models which serve as underlying sets from which each of the three phases is derived. Once the images are segmented, the method is direct and requires no numerical optimization. The 3D models are generated using the covariance function which is measured easily on images. Furthermore, the latter follows quite closely a simple analytical formula which can be used as parametrization. Using the models, preliminary results have been obtained regarding permeability and ionic conductivity. The tools elaborated in this work offer a robust way to study the effect of certain microstructural parameters such as phase volume fractions and length scales on the transport properties.

# Acknowledgement

All the coworkers from the German Aerospace Center (Germany), Alantum Europe GmbH (Germany), CerPoTech AS (Norway), CNR (Italy), Grenoble INP (France), Ceraco GmbH (Germany), Saan Energy AB (Sweden) and ARMINES (France) who have been involved in the framework of the project EVOLVE are gratefully acknowledged for their contribution to this work. This project has received funding from the European Union's Seventh Framework Programme (FP7/2007-2013) for the Fuel Cells and Hydrogen Joint Technology Initiative under grant agreement No. 303429.

# References

[1] C. D. Savaniu, J. T. S. Irvine. Solid State Ionics, **192**(1), 491–493 (2011).

[2] B. Steele. Solid State Ionics, **129**, 95–110 (2000).

[3] B. Abdallah, F. Willot, D. Jeulin. Morphological 3D models of a three-phases SOFC anode microstructure from SEM 2D images. In preparation.

[4] C. Tomasi, R. Manduchi. Proc. 1998 IEE Int. Conf. on Comput. Vision, Bombay, India.

[5] E. Michael. On the origin of the bilateral filter and ways to improve it. IEEE Trans. Image Processing **11**(10), 1141–1151 (2002).

[6] F. Durand, J. Julie Dorsey. Fast bilateral filtering for the display of high-dynamic-range images. ACM Trans. Graphics (TOG) **21**(3), 257–266 (2002).

[7] L. Gillibert, C. Peyrega, D. Jeulin, V. Guipont, M. Jeandin. 3D multiscale segmentation and morphological analysis of X-ray microtomography from cold-sprayed coatings. J. Microscopy **248**(2), 187–199 (2012).

[8] C. Lantuéjoul. Geostatistical Simulation – Models and algorithm, Berlin, pp. 183–240, 2002.

[9] F. Bron, D. Jeulin. Modelling a food microstructure by random sets. Image Analysis & Stereology **23**, 33–44 (2004).

[10] M. Armstrong, A. Galli, H. Beucher, G. Loc'h, D. Renard, B. Doligez, R. Eschard, F. Geffroy. Plurigaussian Simulations in Geosciences, Springer, 2011.

[11] F. Willot, B. Abdallah, Y.-P. Pellegrini. Fourier-based schemes with modified Green operator for computing the electrical response of heterogeneous media with accurate local fields. Int. J. Num. Meth. Engng **98**(7), 518–533 (2014).

[12] A. Wiegmann. Computation of the permeability of porous materials from their microstructure by FFF-Stokes. Berichte des Fraunhofer ITWM **129** (2007).

[13] B. Abdallah, F. Willot, D. Jeulin. Stokes flow through a Boolean model of spheres: Representative volume element. Submitted to Transp. Porous Media.

[14] L. Decker, D. Jeulin, I. Tovena. 3D morphological analysis of the connectivity of a porous medium. Acta Stereo., **17**(1) 107–112 (1998).